High-amplitude effect on Richtmyer–Meshkov instability at a single-mode heavy–light interface ⊕ ✓

He Wang (王何) ⓘ ; Hui Wang (王辉); Zhigang Zhai (翟志刚) ✉ ⓘ ; Xisheng Luo (罗喜胜) ⓘ

Check for updates

View Online   Export Citation

High-amplitude effect on Richtmyer–Meshkov instability at a single-mode heavy–light interface EP

View Online   Export Citation   CrossMark

He Wang (王何),[1] Hui Wang (王辉),[1] Zhigang Zhai (翟志刚),[1,a] and Xisheng Luo (罗喜胜)[1,2]

AFFILIATIONS

[1]Advanced Propulsion Laboratory, Department of Modern Mechanics, University of Science and Technology of China,
 Hefei 230026, China
[2]State Key Laboratory of High Temperature Gas Dynamics, Institute of Mechanics, Chinese Academy of Sciences,
 Beijing 100190, China

[a]Author to whom correspondence should be addressed: sanjing@ustc.edu.cn

ABSTRACT

An experimental study is conducted to explore the high-amplitude effect on Richtmyer–Meshkov instability (RMI) at a single-mode heavy–light interface. A wide range of scaled initial amplitude (ka_0, where k and a_0 are perturbation wavenumber and initial amplitude, respectively) is considered. Qualitatively, nonstandard (standard) indirect phase inversion occurs in experiments with high (low and moderate) ka_0. The nonstandard indirect phase inversion exhibits a complex process, and the interface mixing width does not reduce to near zero. Quantitatively, the linear model poorly (accurately) predicts the post-phase-inversion linear amplitude growth rate when ka_0 is high (low and moderate). Additionally, a representative theoretical reduction factor fortuitously evaluates the high-amplitude effect on the post-phase-inversion linear amplitude growth rate well. The high-amplitude effect significantly alters the nonlinear evolution law, which differs from the case of RMI at a light–heavy interface. None of the considered nonlinear models can accurately predict the amplitude evolution under all ka_0 conditions, regardless of whether their expressions are related to ka_0 or not. Based on the current experimental results, an empirical nonlinear model is proposed to describe RMI at a single-mode heavy–light interface across a wide range of ka_0 conditions.

Published under an exclusive license by AIP Publishing. https://doi.org/10.1063/5.0180581

I. INTRODUCTION

Richtmyer–Meshkov instability (RMI)[1,2] occurs when a corrugated interface separating two fluids of different densities is impulsively accelerated by a shock wave. Understanding RMI-induced perturbation growth and the resulting material mixing is crucial because RMI plays a vital role in various applications such as inertial confinement fusion (ICF),[3–5] supernova explosion,[6,7] and scramjet.[8,9] Comprehensive insights and specific details regarding RMI and its applications can be found in several reviews.[10–13] In ICF, the interface separating ablator and deuterium–tritium (DT) ice and the interface separating DT ice and DT gas are both heavy–light ones. In addition, the initial perturbations on the interfaces in ICF capsule have various scaled initial amplitudes (ka_0, where k and a_0 represent perturbation wavenumber and initial amplitude, respectively). Therefore, it is necessary and desirable to study the evolution of RMI at a heavy–light interface (H-L RMI) under diverse ka_0 conditions. Referring to previous works,[14–16] the initial interface (II) amplitude can reasonably be regarded as low, moderate, and high when $ka_0 \leq 1/3$, $1/3 < ka_0 < 2/3$, and $ka_0 \geq 2/3$, respectively.

For H-L RMI with low and moderate ka_0, Meyer and Blewett[17] performed a numerical study and focused on the early-time evolution. It was found that the impulsive model proposed by Richtmyer[1] predicts the post-phase-inversion linear amplitude growth rate ($\dot{a}_{po}$) poorly. On the basis of the impulsive model and numerical results, Meyer and Blewett[17] proposed a modified linear model for H-L RMI (MB model). Subsequently, Yang et al.[18] derived a compressible linear theory for the low-amplitude H-L RMI (YZS theory) and discussed the parameter conditions corresponding to the two types of phase inversion (i.e., direct and indirect phase inversions). The direct (indirect) phase inversion completes its process at (after) the end of the shock-interface interaction. Experimentally, Meshkov[2] first studied H-L RMI with low and moderate ka_0 (0.31 and 0.63) using interfaces formed by nitrocellulose membrane and obtained $\dot{a}_{po}$. However, no quantitative theory was available to compare with the experimental results at that time. Using well-defined interfaces created by membrane deposited on a stereolithographed grid support, Mariani et al.[19] conducted shock-tube experiments on H-L RMI with ka_0 of 0.24 and 0.36. It was observed that the experimental results are in very good agreement with

08 April 2024 03:52:15

theories[1,20] and simulations. Recently, using the soap-film technique to generate desirable single-mode heavy–light interfaces, Guo et al.[21] studied H-L RMI with low and moderate ka_0 (ranging from 0.16 to 0.63) and provided a direct experimental validation of the MB model.

To understand the high-amplitude effect on H-L RMI, Holmes et al.[22] numerically studied RMI at beryllium-foam interfaces with ka_0 ranging from 0.25 to 3.14 under high-energy-density (HED) conditions. It was observed that the YZS theory and MB model provide reasonable (poor) predictions for the early-time amplitude evolution when ka_0 is low and moderate (high). Moreover, the nonlinear model of Zhang and Sohn,[23] referred to as the ZS model, initiated by the YZS theory reasonably (poorly) predicts the temporal variation of the amplitude growth for H-L RMI with $ka_0 < 2/3$ ($ka_0 > 1.5$). Experimentally, Glendinning et al.[24] investigated RMI induced by a strong laser-driven shock impacting a solid-state heavy–light interface and considered two different initial perturbations with ka_0 of 0.29 and 0.92, respectively. Similarly, the YZS theory only well predicts the early-time evolution of the interface with low ka_0. In addition, for H-L RMI with low ka_0, both the ZS model and the nonlinear model proposed by Sadot et al.[25] (SEA model) can reasonably forecast the nonlinear amplitude evolution. For H-L RMI with $ka_0 = 0.92$, the ZS model (SEA model) still predicts (fails to predict) the nonlinear amplitude growth well.

In the HED experiment, the perturbation evolution is influenced not only by hydrodynamic instabilities but also by the phase transition of the solid materials forming the initial interface,[26] making it difficult to isolate the contribution of RMI to the perturbation growth. In contrast, the shock-tube experiment provides a relatively "simpler" physical environment for the shock-induced interface evolution and, therefore, facilitates the investigation of RMI. Jourdan and Houas[27] experimentally studied H-L RMI with $ka_0 = 1.5$ in a horizontal large-cross section shock tube using interfaces formed by microfilm membrane. The study found that the impulsive model effectively describes the bubble inversion of H-L RMI with low post-shock Atwood number [$A = (\rho_d - \rho_u)/(\rho_d + \rho_u)$, with ρ_d and ρ_u being the densities of fluids at the downstream and upstream sides of the shocked interface (SI), respectively]. In addition, it was found that Vandenboomgaerde's analytic model[20] balanced by a reduction factor (C_r) proposed by Rikanati et al.[28] accurately predicts the nonlinear amplitude evolution of bubble in H-L RMI with high A. However, Jourdan and Houas[27] considered a quasi-single-mode interface that contains non-periodic portions, which, as indicated by Luo et al.,[29] cannot be treated as a single-mode one. Guo et al.[21] investigated high-amplitude H-L RMI ($ka_0 = 1.36$) with reshock, and found that the MB model fails to provide a reasonable prediction for the experimental $\dot{a}_{po}$. However, only one experiment with high ka_0 was conducted, and the emphasis was on the post-reshock flow.

In the previous shock-tube experiments, due to the difficulties encountered in generating a single-mode interface with high ka_0, the related studies are scarce. In our previous work,[30] the soap-film technique was used to generate single-mode air–SF$_6$ interfaces with diverse ka_0, and high-amplitude effect on the RMI at a light–heavy interface (L-H RMI) was highlighted. For H-L RMI, however, some issues remain unclear. How does the high amplitude affect the phase inversion, linear amplitude growth, and nonlinear amplitude evolution? Can existing theories accurately predict the amplitude evolution of H-L RMI under various ka_0 conditions? Does the high-amplitude effect
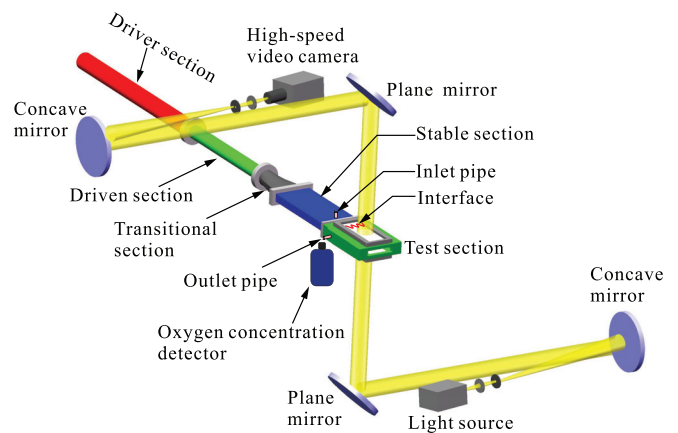

FIG. 1. Sketch of the shock tube and high-speed schlieren system.

in H-L RMI differ from that in L-H RMI? These issues motivate the present study. In this work, the soap-film technique is also used to create well-defined single-mode interfaces with diverse ka_0. The development of H-L RMI under a wide range of ka_0 conditions is obtained through shock-tube experiments. Subsequently, the interface morphology under various ka_0 conditions is discussed. Finally, the pre- and post-phase-inversion amplitude evolutions are analyzed, and a representative theoretical C_r and several typical nonlinear models are examined.

II. EXPERIMENTAL METHODS

To highlight the high-amplitude effect, five experimental cases with the same wavelength (40 mm) but different a_0 (2, 4, 8, 12, and 18 mm) are conducted, with ka_0 of 0.31, 0.63, 1.26, 1.89, and 2.83, respectively. Note that the experimental case will be referred to as case "ka_0," and cases 0.31 and 0.63 serve as reference cases to demonstrate the high-amplitude effect.

In this study, a horizontal shock tube and the soap-film technique, which have been widely verified in our previous works,[30–33] are adopted to generate the shock wave and the initial interface, respectively. The shock tube consists of a driver section, a driven section, a transitional section, a stable section, and a test section, as depicted in Fig. 1. The interface formation devices (devices A and B) shown in Fig. 2 are manufactured by assembling two transparent acrylic plates (5 mm in thickness) with pedestals (6 mm in height). Two identical single-mode-shaped constraint strips are affixed to the pre-carved grooves on device B to constrain the soap film. The height ratio between the constraint strips protruding into the flow field and the entire flow field is 10%, which ensures that the effect of the constraint
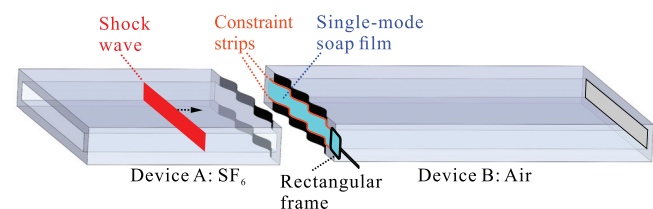

FIG. 2. Schematic of single-mode SF$_6$–air interface formation.

strips on the post-shock flow is negligible.[33] To create a single-mode-shaped soap film, a rectangular frame with the soap solution (78% pure water, 2% sodium oleate, and 20% glycerin by mass) attached is cautiously drawn along the pre-moistened constraint strips. Subsequently, devices A and B are carefully connected and inserted into the test section of the shock tube. For creating an SF_6–air interface, air on the upstream side of the soap film needs to be replaced with SF_6 using the following procedure. First, a thin membrane is used to separate the transitional and stable sections. Then, SF_6 is charged slowly into the stable and test sections through the inlet pipe, and air is released through the outlet pipe. An oxygen concentration detector is placed at the outlet pipe to monitor the oxygen concentration in the test section. Once the volume fraction of oxygen drops below 0.5%, the pipes are removed, and then the holes are sealed. Subsequently, the experiment can be conducted.

The ambient pressure and temperature are 101.3 ± 0.1 kPa and 301.3 ± 1.0 K, respectively. The flow field evolution is captured by a high-speed schlieren system, as depicted in Fig. 1. The frame rate of the high-speed video camera (FASTCAM SA5, Photron Limited) is set to 50 000 fps, with an exposure time of 1 μs. The spatial resolution of the schlieren images is ~ 0.39 mm · pixel^{-1}.

Some significant experimental parameters are listed in Table I. We should point out that it is challenging to ensure that the gas on one side of the interface is pure air or pure SF_6 in experiments. As discussed in previous studies,[34,35] gas is capable of penetrating through the soap–film interface. After the interface is formed and before the experiment is performed, the time interval allows the gas to diffuse through the soap–film interface. As a result, the gases on both sides of the interface are a mixture of SF_6 and air, and the volume fractions of SF_6 on upstream side (VF_1) and downstream side (VF_2) of the initial interface should be first determined. In this work, the volume fractions of SF_6 are determined by solving the shock–interface interaction using one-dimensional gas dynamics theory. Through a MATLAB procedure, the experimental incident shock (IS) velocity (u_i^e) is chosen as an input parameter, and VF_1 and VF_2 are altered to match the experimental transmitted shock (TS) velocity (u_t^e) and its theoretical counterpart while ensuring that the average shock-induced interface velocity (Δv^e) and its theoretical counterpart are in reasonable agreement. Once these two goals are achieved, VF_1 and VF_2 adopted in the procedure are regarded as the corresponding experimental values. In our experiments, u_i^e and u_t^e are obtained by linearly fitting the trajectories of the incident and transmitted shock waves, respectively. Note that the transmitted shock is disturbed, and its trajectory is obtained by averaging the horizontal coordinates of the most upstream and most downstream points on it. In addition, since the interface mean position is regarded as the average of the horizontal coordinates of the spike (heavier fluids penetrating lighter ones) and bubble (lighter fluids penetrating heavier ones), Δv^e is calculated as the average of the velocities of the spike and bubble.

III. RESULTS AND DISCUSSION
A. Flow features and interface morphology

Schlieren images of five experimental cases are provided in Fig. 3. The temporal origin ($t = 0$ μs) is defined as the moment when the incident shock (IS) reaches the balanced position of the single-mode SF_6–air initial interface (II). It is important to note that II appears thick due to the presence of the constraint strips. For clarity, the constraint strips are removed from the images through image processing once the shocked interface (SI) moves away from them. In addition, it can be observed that the right side of the interface does not display a uniform gray background, especially for case 1.89. Although SF_6 would leak from the upstream to the downstream sides of the initial interface, the leakage is limited in our experiments (VF_2 is close to 0.01). The density gradient caused by the leakage of SF_6 should be limited and barely visible using schlieren photography. The non-uniform gray background is possibly caused by the imperfections of the interface formation devices. In experiments, the interface formation devices are manufactured by assembling two transparent acrylic plates with pedestals. Due to the limitation of the machining accuracy, the thickness of the acrylic plate is generally non-uniform, which leads to the non-uniform background captured by schlieren photograph. In addition, some other imperfections on the acrylic plate, such as scratches and attached soap solution, may also lead to the non-uniform background. Some "shadows" can be seen between the transmitted waves and the interface (particularly at the top and bottom of the image corresponding to $t = 199$ μs in case 2.83). Although the non-uniform background does not affect the flow evolution, it hinders the readers from clearly obtaining the effective experimental information. Therefore, during the image post-processing, most of the background non-uniformities were eliminated on the premise of maintaining effective experimental information. In Fig. 3(e), due to the complex shock structures, it is difficult to eliminate all the background non-uniformities while still maintaining the shock structures. Therefore, some background non-uniformities near the shock waves and interface were preserved.

For H-L RMI with low to moderate ka_0, case 0.63 is taken as an example to illustrate the detailed evolution process. As shown in Fig. 3(b), IS would directly intersect with the transmitted shock (TS) during the IS-II interaction (-1 μs), indicating the occurrence of

TABLE I. Some significant parameters for five experimental cases. VF_1 (VF_2): volume fraction of SF_6 on the upstream (downstream) side of the initial interface; A: post-shock Atwood number; u_i^e and u_t^e: velocities of the incident and transmitted shocks obtained from experiments, respectively; Δv^e and Δv^t: shock-induced interface velocities measured from experiments and predicted by one-dimensional gas dynamics theory, respectively; v_{tip}^e and v_{bt}: experimental spike tip velocity and its fraction induced by baroclinic vorticity, respectively.

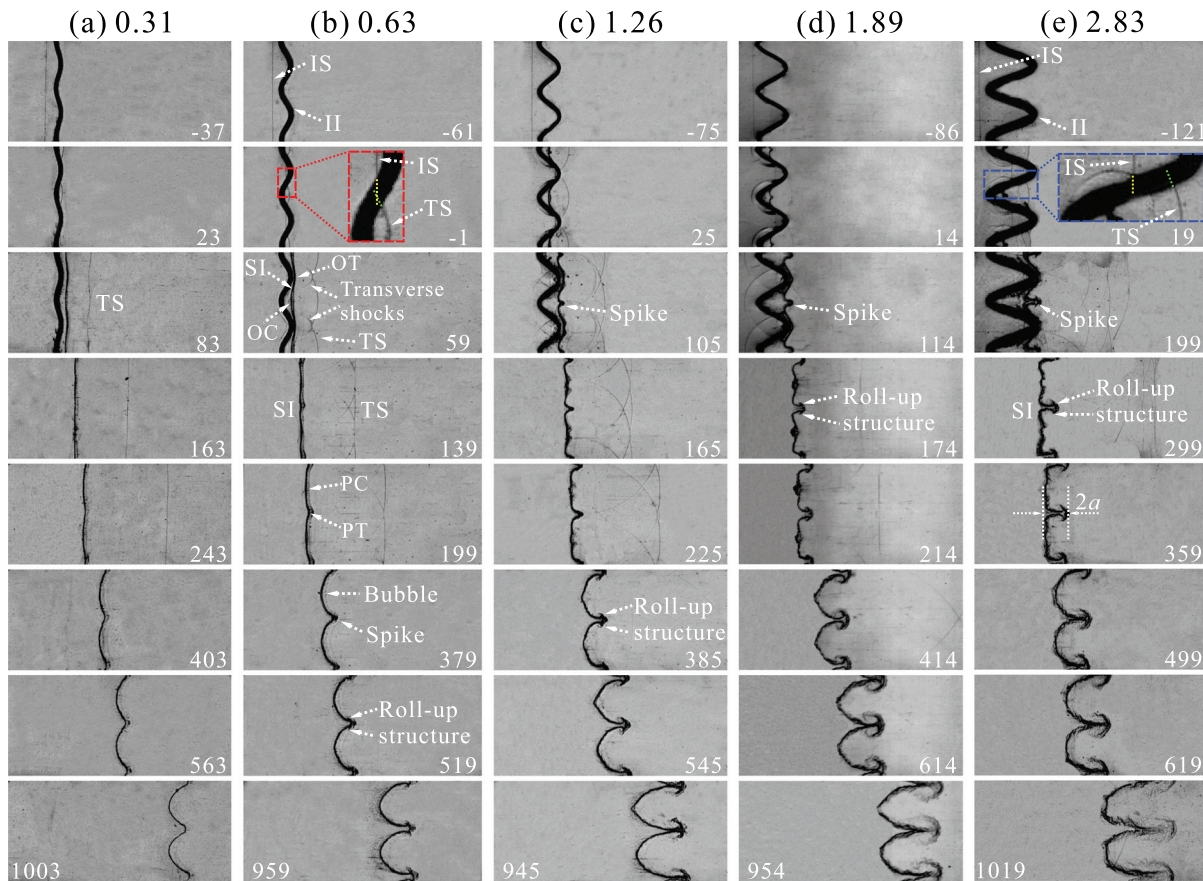| Case	VF_1	VF_2	A	u_i^e (m/s)	u_t^e (m/s)	Δv^e (m/s)	Δv^t (m/s)	v_{tip}^e (m/s)	v_{bt} (m/s)	$v_{bt}/\Delta v^e$ (%)
0.31	0.81	0.01	-0.63	192.5	399.7	93.8	93.2	102.8	9.0	9.6
0.63	0.90	0.01	-0.66	182.6	396.9	89.5	90.9	112.4	22.9	25.6
1.26	0.83	0.01	-0.63	188.3	395.4	89.3	89.3	126.0	36.7	41.2
1.89	0.91	0.02	-0.64	182.9	386.9	91.1	90.9	138.6	47.5	52.1
2.83	0.84	0.02	-0.62	187.9	384.2	87.4	87.5	148.6	61.2	70.1

FIG. 3. Schlieren photographs of the evolutions of shocked single-mode SF_6–air interfaces with different ka_0. IS: incident shock; II: initial interface; TS: transmitted shock; SI: shocked interface; OT and OC (PT and PC): original (post-phase-inversion) trough and crest, respectively. Yellow and green dotted lines are the extension lines of observed IS and TS, respectively. Numbers represent time in μs.

regular refraction.[36] The baroclinic vorticity generated due to the misalignment of the pressure and density gradients induces downstream-directed and upstream-directed velocities at the original crest and trough of SI (OC and OT), respectively. Consequently, the perturbation amplitude (a), defined as half of the distance between the two points OC and OT along the streamwise direction, decreases continuously after the IS-II interaction (59–139 μs). In H-L RMI with low to moderate ka_0, the mixing width (w), defined as the distance between the most upstream and most downstream points on SI along the streamwise direction, is close to a and also reduces gradually after the IS-II interaction. A standard indirect phase inversion occurs at approximately $t = 139$ μs, with both a and w reducing to nearly zero. Subsequently, OC and OT transform into the post-phase-inversion trough and crest (PT and PC), respectively (199 μs). After the phase inversion, the perturbation amplitude is defined as half of the distance between PC and PT along the streamwise direction. To avoid confusion, both OC and PT (OT and PC) are referred to below as spike (bubble) tip. After the phase inversion, the asymmetry of SI increases gradually, followed by the formation of distinct spike and bubble structures (379 μs), indicating the generation of high-order harmonics. Subsequently, roll-up structures are formed on SI (519 μs).

The overall flow features in case 0.31 are similar to those in case 0.63. However, there are still some differences. In case 0.31, since the perturbation of TS imprinted by II is limited, TS maintains a smooth morphology throughout its evolution process. In contrast, in case 0.63, the perturbation of TS imprinted by II is relatively large, and TS rapidly evolves into a series of Mach reflection configurations (59 μs). The reflected shocks in the Mach reflection configurations, also known as transverse shock waves, will continuously affect the interface evolution and introduce the secondary compression effect. Specifically, the secondary compression effect includes the direct interaction of the transverse shocks with SI and the effect of the high-pressure zones created by the intersection of transverse shocks. Furthermore, due to the small initial perturbation amplitude, SI in case 0.31 evolves slowly, and no roll-up structures are formed on it within the effective experimental time.

Case 2.83 is taken as an example to illustrate the detailed evolution process of high-amplitude H-L RMI. As shown in Fig. 3(e), IS does not directly intersect with TS during the IS-II interaction (19 μs), indicating the occurrence of irregular refraction.[36] Compared to H-L RMI with low to moderate ka_0, the average angle between IS and II is larger in high-amplitude H-L RMI, resulting in more baroclinic

vorticity deposited on SI and, accordingly, higher baroclinic-vorticity-induced velocity (v_{bv}). Due to the high downstream-directed v_{bv} near the spike tip and the prolonged duration of the IS-II interaction, SI near the spike tip inverts before the IS-II interaction ends (19 μs). As a result, w in high-amplitude H-L RMI would not reduce to nearly zero. Due to the high upstream-directed v_{bv} near the bubble tip, SI near the bubble tip inverts shortly after the IS-II interaction (299 μs). Meanwhile, the roll-up structures are formed on the spike tip. We may refer to this type of phase inversion as nonstandard indirect phase inversion to differentiate it from the standard one. After the spike and bubble tips become the most downstream and most upstream points on SI, respectively, the evolution of SI follows the same tendency as that in H-L RMI with low to moderate ka_0, but the nonlinear evolution features of SI develop faster. In the late stages, the stem of the spike becomes very slender (499–1019 μs), which differs from the cases of H-L RMI with low to moderate ka_0 and high-amplitude L-H RMI.[30]

The overall flow features in cases 1.26 and 1.89 are similar to those in case 2.83. In the case with higher ka_0, the thinning of the spike stem and the development of the roll-up structures are more rapid, which should be attributed to more baroclinic vorticity deposition on SI. At late stages, the decomposition of the roll-up structures caused by the secondary instability[37] is apparent in cases 1.89 and 2.83. This would result in the generation of local mixing zones on both sides of the spike stem.[37,38] In contrast, in case 1.26, the decomposition of the roll-up structures and the resulting mixing appear to be still limited at late stages. Note that in Secs. III B–III D, the moment of the phase inversion is defined as the moment when $a = 0$ to avoid confusion and facilitate analysis.

B. Spike tip velocity

The movements of the spike tip for different cases are provided in Fig. 4, in which x is the coordinate along the streamwise direction, and x_i and t_i denote the x coordinate and moment of the first extracted data, respectively. Note that the error bars describe the uncertainty in extracting the position of th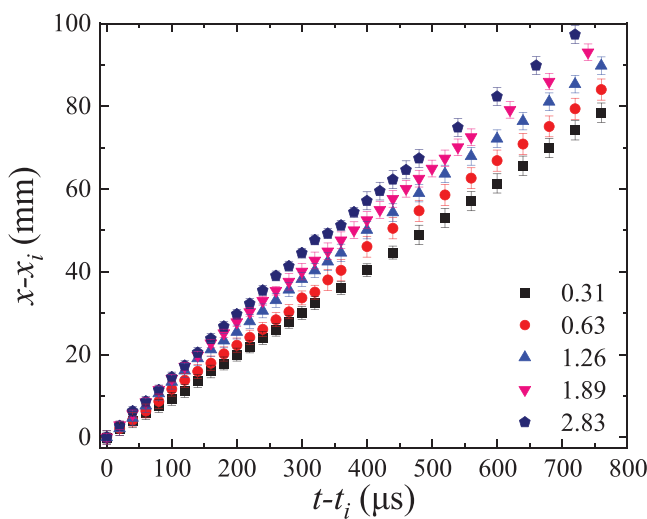e spike tip from experiments because the interface has a thickness. The spike tip moves almost linearly in all cases, with greater velocity in cases with higher ka_0. The flow field of RMI can be divided into two parts: a uniform background flow field and a non-uniform perturbed flow field. The velocity of the perturbed flow field is induced by baroclinic vorticity deposited by shock waves, and the velocity of the background flow is Δv^e. Accordingly, the velocity of the spike tip measured in the laboratory coordinate system (v_{tip}^e) is a superposition of Δv^e and the velocity of the perturbed flow field at the spike tip (v_{bt}): $v_{tip}^e = \Delta v^e + v_{bt}$. Since v_{bt} is physically induced by baroclinic vorticity, it represents exactly the fraction of v_{tip}^e induced by baroclinic production. v_{tip}^e, v_{bt}, and $v_{bt}/\Delta v^e$ for different cases are listed in Table I. v_{bt} exhibits a strong positive correlation with ka_0, and $v_{bt}/\Delta v^e$ exceeds 40% when $ka_0 \geq 1.26$.

During the penetration of the spike, the spike tip needs to push away the lighter fluid in front of it, thus suffering a reacting force that causes its velocity to decrease. Accordingly, if v_{bt}, which also denotes the velocity of the spike tip with respect to the background flow, is higher, the spike would be capable of penetrating deeper into the lighter fluid. In other words, the penetrating capability of the spike is directly influenced by v_{bt}, which is strongly positively related to ka_0. As a result, it is essential to minimize high-amplitude perturbations on the interfaces of ICF target to prevent the ingress of ablative material into the hot spot.

C. Pre- and post-phase-inversion linear amplitude evolutions

The temporal variations of perturbation amplitude a for different cases are shown in Fig. 5 in dimensional form, in which t_* is the moment corresponding to the smallest post-phase-inversion amplitude extracted from experiments (a_*). The overall amplitude evolution can be divided into three stages, including the pre-phase-inversion linear stage (stage I), post-phase-inversion linear stage (stage II), and post-phase-inversion nonlinear stage (stage III). The experimental pre-
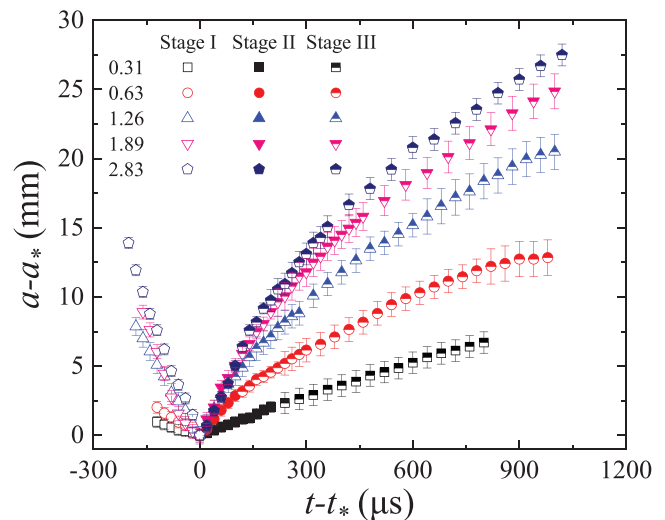
FIG. 4. Movements of the spike tip for different cases.

FIG. 5. Temporal variations of perturbation amplitude. Stage I: pre-phase-inversion linear stage; stage II: post-phase-inversion linear stage; and stage III: post-phase-inversion nonlinear stage.

and post-phase-inversion linear amplitude growth rates ($\dot{a}_{pr}^e$ and $\dot{a}_{po}^e$) are obtained by linearly fitting the temporal variations of amplitude within stages I and II, respectively. Relevant results are provided in Table II. For cases with low to moderate ka_0, $\dot{a}_{pr}^e$ is lower than $\dot{a}_{po}^e$. According to the linear compressible theory of RMI,[1,18] the early-time evolution of the interface is driven by the pressure perturbations caused by the distorted transmitted and reflected waves in the vicinity of the interface. The continuous effect of the pressure perturbations causes the amplitude growth rate to increase in an oscillatory manner toward a maximum value. This process is generally referred to as the startup period.[39] Since the phase-inversion process is short in cases with low to moderate ka_0, the smaller $\dot{a}_{pr}^e$ than $\dot{a}_{po}^e$ is likely because the amplitude evolution is still within the startup period when phase inversion occurs. For cases with high ka_0, due to the relatively long duration of the phase-inversion process, the effect of the startup process on the post-phase-inversion amplitude evolution should be weak. $\dot{a}_{po}^e$ is smaller than $\dot{a}_{pr}^e$, which should be attributed to the nonlinear effect, as evidenced by the significant nonlinear features of the post-phase-inversion interface shown in Fig. 3. In other words, the interface evolution in stage II of high-amplitude H-L RMI has a linear imprint on the amplitude growth even if it corresponds to a nonlinear physical process.

The MB model,[17] which has been validated numerically[22] and experimentally[21] in predicting $\dot{a}_{po}$ of low-amplitude H-L RMI, is employed to provide a theoretical reference for $\dot{a}_{po}^e$ under diverse ka_0 conditions. The MB model can be described as

$$\dot{a}_{mb} = k\Delta v^e A \frac{(1 + C_c)a_0}{2}, \tag{1}$$

in which $C_c = 1 - \Delta v^e / u_i^e$ is the shock-compression factor. For cases with low to moderate ka_0, $\dot{a}_{po}^e$ agrees well with $\dot{a}_{mb}$, with a difference of less than 7%. However, the discrepancy between $\dot{a}_{po}^e$ and $\dot{a}_{mb}$ is greater in cases with higher ka_0 due to the more significant high-amplitude and nonlinear effects.

To evaluate the high-amplitude effect on the linear amplitude growth rate, several different theoretical C_r have been proposed.[28,40–42] Since the differences between their values are very limited,[30] only the theoretical C_r proposed by Dimonte and Ramaprabhu[40] (C_{dr}) is adopted in this work as a representative one. Comparison between the experimental C_r of H-L RMI ($C_{h-l} = \dot{a}_{po}^e / \dot{a}_{mb}$) and C_{dr} is given in Fig. 6. C_{h-l} exhibits reasonable agreement with C_{dr}, which, however, could be fortuitous because the additional nonlinearity introduced by the phase-inversion process and the secondary compression effect caused by transverse waves[30,43] were not considered when constructing C_{dr}.

TABLE II. Experimental and theoretical results of the linear amplitude growth rate. $\dot{a}_{pr}^e$ and $\dot{a}_{po}^e$: experimental pre- and post-phase-inversion linear amplitude growth rates, respectively; $\dot{a}_{mb}$: linear amplitude growth rate predicted by the MB model.

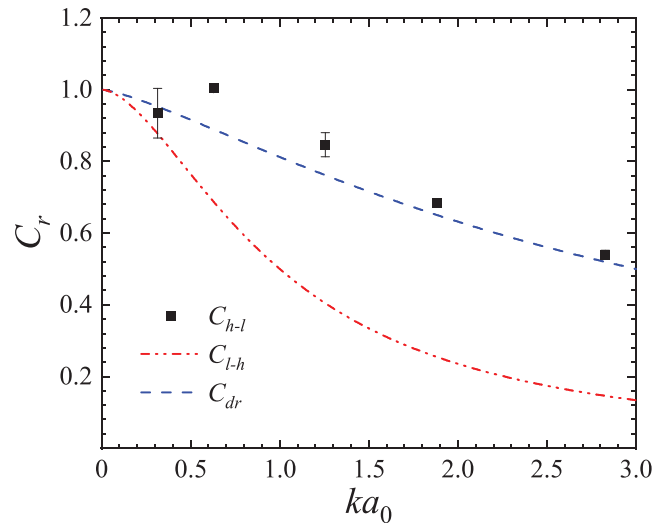| Case	$\dot{a}_{pr}^e$ (m/s)	$\dot{a}_{po}^e$ (m/s)	$\dot{a}_{mb}$ (m/s)
0.31	9.23 ± 0.49	13.11 ± 0.97	14.03
0.63	25.02 ± 1.01	28.00 ± 0.13	27.89
1.26	47.68 ± 1.14	45.94 ± 1.82	54.27
1.89	65.46 ± 0.93	56.75 ± 0.72	82.97
2.83	73.32 ± 1.72	63.05 ± 1.48	116.83

FIG. 6. Comparison between experimental C_r of H-L RMI (C_{h-l}), empirical C_r proposed based on experimental results of L-H RMI[30] (C_{l-h}) and theoretical C_r proposed by Dimonte and Ramaprabhu[40] (C_{dr}).

For exploring the similarities and differences in the high-amplitude effect between H-L and L-H RMI, C_{h-l} is compared with the empirical C_r proposed based on the experimental results of L-H RMI (C_{l-h}),[30] as shown in Fig. 6. It is worth mentioning that the most notable distinction between H-L and L-H RMI lies in that the former has a phase-inversion process. C_{h-l} for case 0.31 agrees reasonably with C_{l-h}. However, C_{h-l} for the other cases deviate significantly from C_{l-h}, suggesting that the high-amplitude effect in H-L RMI differs from that in L-H RMI. The separation of TS from SI occurs faster in H-L RMI compared to that in L-H RMI and, accordingly, the secondary compression effect in H-L RMI should be weaker than that in L-H RMI. Hence, the existence of phase-inversion process in H-L RMI and the difference in the secondary compression effect are likely the main reasons for the difference in the high-amplitude effects between H-L and L-H RMI.

D. Post-phase-inversion nonlinear amplitude growth

As nonlinearity becomes further significant, amplitude growth enters stage III. The temporal variations of post-phase-inversion a in dimensionless form for cases with different ka_0 are shown in Fig. 7, in which t and a are normalized as $\tau = k\dot{a}_{po}^e(t - t_*)$ and $\alpha = k(a - a_*)$, respectively. The scaling approach fails to collapse the results of different cases, indicating that the high-amplitude effect also influences the nonlinear evolution law. Notably, the same scaling approach collapses the results of experiments on L-H RMI with various ka_0,[30] which further demonstrates that the high-amplitude effects in H-L and L-H RMI are different. The additional nonlinearity introduced by the phase-inversion process to the post-phase-inversion amplitude evolution, as observed in Subsection III C, is significantly different for H-L RMI with different ka_0, which explains the differences in evolution law between cases. Moreover, this additional nonlinearity is likely the primary factor causing the distinct dependencies of the nonlinear evolution law on ka_0 for H-L and L-H RMI.
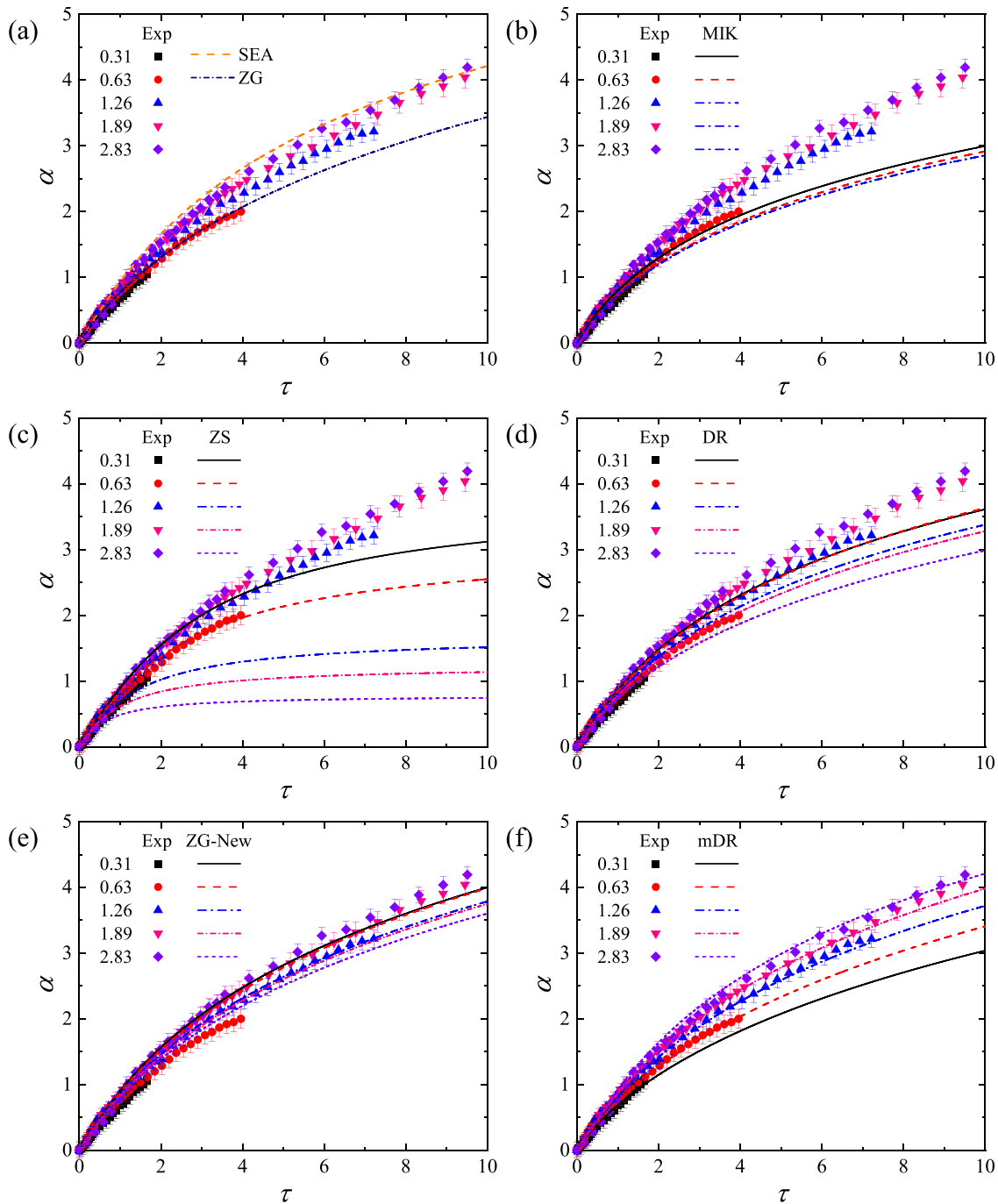
FIG. 7. Comparisons between post-phase-inversion nonlinear amplitude evolutions in dimensionless form obtained from experiments and predicted by nonlinear models. (a) SEA and ZG models; (b) MIK model; (c) ZS model; (d) DR model; (e) ZG-New model; and (f) mDR model. Symbols and lines represent the experimental results and theoretical predictions, respectively.

Subsequently, a comparative analysis of the experimental results and predictions by typical nonlinear models is performed. Nonlinear models including the ZS,[23] MIK,[44] SEA,[25] DR,[40] ZG,[45] and ZG-New[46] models are considered, and their detailed expressions are listed in Table III. The SEA and ZG models do not consider the effect of the initial amplitude, and their predictions are compared with the experimental results in Fig. 7(a). Notably, the predictions of the SEA and ZG models for various cases are slightly different due to the discrepancies

TABLE III. Detailed expressions of considered nonlinear models, in which subscripts "b" and "s" represent bubble and spike, respectively.

Model	Expression
ZS	$$\dot{a}^{ZS}_{b/s} = \dot{a}^{ZS} \mp \frac{|A|k\dot{a}^{e}_{po}{}^{2}t}{1 + 2k^2 C_c a_0 \dot{a}^e_{po} t + 4k^2 \dot{a}^e_{po}{}^2 t^2 \left[(C_c ka_0)^2 + \frac{1}{3}(1 - A^2) \right]},$$ in which $\dot{a}^{ZS} = \dfrac{\dot{a}^e_{po}}{1 + k^2 C_c a_0 \dot{a}^e_{po} t + \max\left[0, (C_c ka_0)^2 - A^2 + \frac{1}{2}\right] k^2 \dot{a}^e_{po}{}^2 t^2}.$
MIK	$\dot{a}^{MIK}_{b/s} = \dot{a}^e_{po}$ when $ka < 1/3$, $\dot{a}^{MIK}_{b/s} = \dfrac{\dot{a}^e_{po}}{1 + 3\dot{a}^e_{po}\left(\frac{1 \pm |A|}{3 \pm |A|}\right)kt}$ when $ka \geq 1/3$.
SEA	$\dot{a}^{SEA}_{b/s} = \dot{a}^e_{po}\dfrac{1 + k\dot{a}^e_{po}t}{1 + (1 \pm |A|)k\dot{a}^e_{po}t + \left(\frac{1 \pm |A|}{1 + |A|}\right)\left(\frac{k^2 \dot{a}^e_{po}{}^2 t^2}{2\pi\eta}\right)}$, in which $\eta = \dfrac{1}{3\pi}$ when $|A| \geq 0.5$ and $\eta = \dfrac{1}{2\pi}$ when $|A| \to 0$.
DR	$\dot{a}^{DR}_{b/s} = \dot{a}^e_{po}\dfrac{1 + (1 \mp |A|)k\dot{a}^e_{po}t}{1 + \delta_{b/s}k\dot{a}^e_{po}t + (1 \mp |A|)F_{b/s}(k\dot{a}^e_{po}t)^2}$, in which $\delta_{b/s} = \dfrac{4.5 \pm |A| + (2 \mp |A|)C_c ka_0}{4}$ and $F_{b/s} = 1 \pm |A|$.
ZG	$\dot{a}^{ZG}_{b/s} = \dfrac{\dot{a}^e_{po}}{1 + \theta_{b/s}k\dot{a}^e_{po}t}$, in which $\theta_{b/s} = \dfrac{3}{4}\dfrac{(1 \pm |A|)(3 \pm |A|)}{3 \pm |A| + \sqrt{2(1 \pm |A|)}}\dfrac{4(3 \pm |A|) + \sqrt{2}(9 \pm |A|)(1 \pm |A|)^{1/2}}{(3 \pm |A|)^2 + 2\sqrt{2}(3 \mp |A|)(1 \pm |A|)^{1/2}}.$
ZG-New	$$\dot{a}^{ZGN}_{b/s} = \dot{a}^e_{po}e^{-k[a_{b/s}(t) - C_c a_0]\theta_{b/s}}\left\{ \frac{\frac{1}{3(\theta_{b/s} \mp |A|)^2}\left(1 + \frac{2C_c ka_0}{\theta_{b/s} \mp |A|}\right) + \lambda_{b/s}}{\frac{1}{3(\theta_{b/s} \mp |A|)^2}\left(1 + \frac{2C_c ka_0}{\theta_{b/s} \mp |A|}\right) + \lambda_{b/s}e^{-3k[a_{b/s}(t) - C_c a_0]}} \right\}^{\frac{1}{3\lambda_{b/s}}}, \text{ in which}$$ $$\lambda_{b/s} = \left[\frac{1}{\theta_{b/s} \mp |A|} - \frac{1}{3(\theta_{b/s} \mp |A|)^2}\right] + \left[\frac{1}{(\theta_{b/s} \mp |A|)^2} - \frac{2}{3(\theta_{b/s} \mp |A|)^3}\right]C_c ka_0.$$

in parameters other than ka_0, and only the middle one among the five theoretical lines is provided for clarity. The SEA model overestimates the results of all cases except case 2.83, which should be attributed to its overestimation of the spike acceleration.[40] The relatively good predictive capability of the SEA model for case 2.83 should be due to the overestimation of the spike acceleration coincidentally describing the high-amplitude effect under this specific ka_0. The ZG model reasonably predicts the experimental results of H-L RMI with low to moderate ka_0 but underestimates the results of high-amplitude H-L RMI from the early times.

The MIK model has different expressions under different ka conditions, thus implicitly describing the effect of the initial amplitude. For cases with low to moderate initial amplitude, $C_c ka_0$ is smaller than 1/3 and the prediction of the MIK model is related to the initial amplitude. The predictions of the MIK model for high-amplitude cases are unrelated to ka_0, but slightly different due to the discrepancies in parameters other than ka_0. Only the middle one among the three theoretical lines of high-amplitude cases is provided in Fig. 7(b) for clarity. The ZS, DR, and ZG-New models are explicitly related to ka_0, and the comparisons between their predictions and the experimental results are shown in Figs. 7(c)–7(e), respectively. Interestingly, the predictions of the ZS, DR, and ZG-New models (MIK model) exhibit a negative correlation with ka_0 (initial amplitude when $C_c ka_0 < 1/3$), whereas the experimental results show a positive dependence on ka_0. When

constructing the MIK, ZS, DR, and ZG-New models, only the linear and nonlinear amplitude growth periods were considered, while the phase-inversion process was not taken into account. The additional nonlinearity introduced by the phase inversion may be the reason why these models fail to describe the dependence of the nonlinear evolution law of H-L RMI on ka_0. Among these models, the ZS model exhibits the poorest predictive performance, and this can be attributed to two reasons. First, in all cases, $\sqrt{1/2 + (C_c ka_0)^2}$ is greater than $|A|$ and, therefore, the asymptotic $\dot{a}$ predicted by the ZS model satisfies the $1/t^2$ law. However, according to the potential flow model prediction and previous numerical and experimental works,[40,47] the late-time behavior of $\dot{a}$ is expected to follow a $1/t$ law. Second, as pointed out by Dimonte and Ramaprabhu,[40] the ZS model exhibits an excessive dependency on ka_0.

The phase-inversion process is complex when ka_0 is high, and its effect on the post-phase-inversion perturbation evolution is hard to describe. Consequently, it is difficult to provide a rigorous theoretical description for the dependence of the nonlinear evolution law of H-L RMI on ka_0. In this study, we attempt to propose an empirical model applicable to H-L RMI across a wide range of ka_0 conditions based on the current experimental results. Among models explicitly describing the dependence on ka_0, the ZS model fails to capture the late-time $1/t$ behavior of $\dot{a}$ when $\sqrt{1/2 + (C_c ka_0)^2} > |A|$, while the ZG-New

model has a rather complex formula. In contrast, the DR model not only captures the late-time $1/t$ behavior of $\dot{a}$ but also has a relatively simple form. Therefore, we shall construct a new empirical model (mDR model) by modifying the DR model. The differences between the DR and mDR models lie in coefficients $\delta_{b/s}$ and $F_{b/s}$. In the mDR model, $\delta_{b/s}$ and $F_{b/s}$ are modified as $[(5\pm|A|)/4 - 3/5\ln(C_c ka_0)]$ and $0.8(1\pm|A|)$, respectively. As shown in Fig. 7(f), the mDR model predicts well the post-phase-inversion amplitude evolution of H-L RMI with ka_0 ranging from 0.31 to 2.83.

IV. CONCLUSIONS

The high-amplitude effect on Richtmyer–Meshkov instability (RMI) at a single-mode heavy–light interface (referred to as H-L RMI) is finely studied through shock-tube experiments, considering a wide range of scaled initial amplitude (ka_0). Qualitatively, nonstandard (standard) indirect phase inversion, whose process is rather complex (simple), occurs at the interface with high (low to moderate) ka_0. In the late stages, the spike stem in high-amplitude H-L RMI becomes very slender, which differs from the cases of H-L RMI with low to moderate ka_0 and RMI at a single-mode light–heavy interface (L-H RMI) with high ka_0.

Quantitatively, the velocity at the spike tip is found to exhibit a strong positive correlation with ka_0. This proves the importance of minimizing initial perturbations on the interfaces of ICF target to prevent the formation of intense spikes that could affect the ignition. In H-L RMI with low to moderate ka_0, the pre-phase-inversion linear amplitude growth rate in experiment is smaller than the post-phase-inversion one due to the startup process. In H-L RMI with high ka_0, however, the post-phase-inversion value is smaller due to the nonlinearity and high-amplitude effect. The existing theoretical reduction factor evaluates the high-amplitude effect, which, however, should be fortuitous because nonlinearity introduced by the phase inversion process and the secondary compression effect were not considered when the reduction factor was proposed.

For the post-phase-inversion nonlinear amplitude growth, a widely used scaling approach fails to collapse the experimental results with different ka_0, indicating that the high amplitude also influences the nonlinear evolution law. None of the considered nonlinear models are found to apply to H-L RMI under all ka_0 conditions, regardless of whether their expressions are related to ka_0 or not. Based on the current experimental results, an empirical nonlinear model applicable to H-L RMI over a wide range of ka_0 conditions is proposed. The present study demonstrates that the high-amplitude effect on the linear and nonlinear evolution laws of perturbation amplitude in H-L RMI differs from that in L-H RMI. This difference is probably attributed to the presence of phase-inversion process in H-L RMI and to the difference in the secondary compression effect between H-L and L-H RMI.

Practically, the perturbations on the interfaces in ICF capsule are generally multi-mode ones instead of single-mode ones. Therefore, investigating RMI on a high-amplitude multi-mode light–heavy/ heavy–light interface is also necessary and interesting. In the following studies, relevant shock-tube experiments will be conducted to explore the coupling of the high-amplitude and mode-coupling/competition effects.

ACKNOWLEDGMENTS

AUTHOR DECLARATIONS
Conflict of Interest

The authors have no conflicts to disclose.

Author Contributions

He Wang: Writing – original draft (lead). **Hui Wang:** Data curation (lead). **Zhigang Zhai:** Supervision (equal); Writing – review & editing (lead). **Xisheng Luo:** Funding acquisition (equal); Supervision (equal).

DATA AVAILABILITY

The data that support the findings of this study are available from the corresponding author upon reasonable request.

REFERENCES

[1] R. D. Richtmyer, "Taylor instability in shock acceleration of compressible fluids," Commun. Pure Appl. Math. **13**, 297–319 (1960).

[2] E. E. Meshkov, "Instability of the interface of two gases accelerated by a shock wave," Fluid Dyn. **4**, 101–104 (1972).

[3] J. Nuckolls, L. Wood, A. Thiessen, and G. Zimmerman, "Laser compression of matter to super-high densities: Thermonuclear (CTR) applications," Nature **239**, 139–142 (1972).

[4] J. Lindl, O. Landen, J. Edwards, and E. Moses, and NIC Team, "Review of the national ignition campaign 2009–2012," Phys. Plasmas **21**, 020501 (2014).

[5] R. Betti and O. A. Hurricane, "Inertial-confinement fusion with lasers," Nat. Phys. **12**, 435–448 (2016).

[6] W. D. Arnett, J. N. Bahcall, R. P. Kirshner, and S. E. Woosley, "Supernova 1987A," Annu. Rev. Astron. Astrophys. **27**, 629–700 (1989).

[7] C. C. Kuranz *et al.*, "How high energy fluxes may affect Rayleigh-Taylor instability growth in young supernova remnants," Nat. Commun. **9**, 1564 (2018).

[8] J. Yang, T. Kubota, and E. E. Zukoski, "Applications of shock-induced mixing to supersonic combustion," AIAA J. **31**, 854–862 (1993).

[9] F. S. Billig, "Research on supersonic combustion," J. Propuls. Power **9**, 499–514 (1993).

[10] Y. Zhou, "Rayleigh-Taylor and Richtmyer-Meshkov instability induced flow, turbulence, and mixing. I," Phys. Rep. **720–722**, 1–136 (2017).

[11] Y. Zhou, "Rayleigh-Taylor and Richtmyer-Meshkov instability induced flow, turbulence, and mixing. II," Phys. Rep. **723–725**, 1–160 (2017).

[12] Y. Zhou, T. T. Clark, D. S. Clark, S. G. Glendinning, M. A. Skinner, C. M. Huntington, O. A. Hurricane, A. M. Dimits, and B. A. Remington, "Turbulent mixing and transition criteria of flows induced by hydrodynamic instabilities," Phys. Plasmas **26**, 080901 (2019).

[13] Y. Zhou, R. Williams, P. Ramaprabhu, M. Groom, B. Thornber, A. Hillier, W. Mostert, B. Rollin, S. Balachandar, P. Powell, A. Mahalov, and N. Attal, "Rayleigh-Taylor and Richtmyer-Meshkov instabilities: A journey through scales," Physica D **423**, 132838 (2021).

[14] M. Vandenboomgaerde, D. Souffland, C. Mariani, L. Biamino, G. Jourdan, and L. Houas, "An experimental and numerical investigation of the dependency on the initial conditions of the Richtmyer-Meshkov instability," Phys. Fluids **26**, 024109 (2014).

[15] Z. Dell, R. F. Stellingwerf, and S. I. Abarzhi, "Effect of initial perturbation amplitude on Richtmyer-Meshkov flows induced by strong shocks," Phys. Plasmas **22**, 092711 (2015).

[16] L. Liu, Y. Liang, J. Ding, N. Liu, and X. Luo, "An elaborate experiment on the single-mode Richtmyer-Meshkov instability," J. Fluid Mech. **853**, R2 (2018).

[17] K. A. Meyer and P. J. Blewett, "Numerical investigation of the stability of a shock-accelerated interface between two fluids," Phys. Fluids **15**, 753–759 (1972).

[18] Y. Yang, Q. Zhang, and D. H. Sharp, "Small amplitude theory of Richtmyer-Meshkov instability," Phys. Fluids **6**, 1856–1873 (1994).

[19] C. Mariani, M. Vandenboomgaerde, G. Jourdan, D. Souffland, and L. Houas, "Investigation of the Richtmyer-Meshkov instability with stereolithographed interfaces," Phys. Rev. Lett. **100**, 254503 (2008).

[20] M. Vandenboomgaerde, in Proceedings of 9th International Workshop on the Physics of Compressible Turbulent Mixing, Cambridge, UK, 2004.

[21] X. Guo, T. Si, Z. Zhai, and X. Luo, "Large-amplitude effects on interface perturbation growth in Richtmyer-Meshkov flows with reshock," Phys. Fluids **34**, 082118 (2022).

[22] R. L. Holmes, G. Dimonte, B. Fryxell, M. L. Gittings, J. W. Grove, M. Schneider, D. H. Sharp, A. L. Velikovich, R. P. Weaver, and Q. Zhang, "Richtmyer-Meshkov instability growth: Experiment, simulation and theory," J. Fluid Mech. **389**, 55–79 (1999).

[23] Q. Zhang and S. I. Sohn, "Nonlinear theory of unstable fluid mixing driven by shock wave," Phys. Fluids **9**, 1106–1124 (1997).

[24] S. G. Glendinning, J. Bolstad, D. G. Braun, M. J. Edwards, W. W. Hsing, B. F. Lasinski, H. Louis, A. Miles, J. Moreno, T. A. Peyser, B. A. Remington, H. F. Robey, E. J. Turano, C. P. Verdon, and Y. Zhou, "Effect of shock proximity on Richtmyer-Meshkov growth," Phys. Plasmas **10**, 1931–1936 (2003).

[25] O. Sadot, L. Erez, U. Alon, D. Oron, L. A. Levin, G. Erez, G. Ben-Dor, and D. Shvarts, "Study of nonlinear evolution of single-mode and two-bubble interaction under Richtmyer-Meshkov instability," Phys. Rev. Lett. **80**, 1654–1657 (1998).

[26] G. Malamud, C. A. Di Stefano, Y. Elbaz, C. M. Huntington, C. C. Kuranz, P. A. Keiter, and R. P. Drake, "A design of a two-dimensional, multimode RM experiment on OMEGA-EP," High Energy Dens. Phys. **9**, 122–131 (2013).

[27] G. Jourdan and L. Houas, "High-amplitude single-mode perturbation evolution at the Richtmyer-Meshkov instability," Phys. Rev. Lett. **95**, 204502 (2005).

[28] A. Rikanati, D. Oron, O. Sadot, and D. Shvarts, "High initial amplitude and high Mach number effects on the evolution of the single-mode Richtmyer-Meshkov instability," Phys. Rev. E **67**, 026307 (2003).

[29] X. Luo, Y. Liang, T. Si, and Z. Zhai, "Effects of non-periodic portions of interface on Richtmyer-Meshkov instability," J. Fluid Mech. **861**, 309–327 (2019).

[30] H. Wang, H. Wang, Z. Zhai, and X. Luo, "High-amplitude effect on single-mode Richtmyer-Meshkov instability of a light-heavy interface," Phys. Fluids **35**, 016106 (2023).

[31] X. Guo, Z. Zhai, J. Ding, T. Si, and X. Luo, "Effects of transverse shock waves on early evolution of multi-mode chevron interface," Phys. Fluids **32**, 106101 (2020).

[32] L. Feng, J. Xu, Z. Zhai, and X. Luo, "Evolution of shock-accelerated double-layer gas cylinder," Phys. Fluids **33**, 086105 (2021).

[33] H. Wang, H. Wang, Z. Zhai, and X. Luo, "Effects of obstacles on shock-induced perturbation growth," Phys. Fluids **34**, 086112 (2022).

[34] T. Si, Z. Zhai, J. Yang, and X. Luo, "Experimental investigation of reshocked spherical gas interfaces," Phys. Fluids **24**, 054101 (2012).

[35] M. Wang, T. Si, and X. Luo, "Experimental study on the interaction of planar shock wave with polygonal helium cylinders," Shock Waves **25**, 347–355 (2015).

[36] A. M. Abd-El-Fattah and L. F. Henderson, "Shock waves at a slow-fast gas interface," J. Fluid Mech. **89**, 79–95 (1978).

[37] G. Peng, N. J. Zabusky, and S. Zhang, "Vortex-accelerated secondary baroclinic vorticity deposition and late-intermediate time dynamics of a two-dimensional Richtmyer-Meshkov interface," Phys. Fluids **15**, 3730–3744 (2003).

[38] R. V. Morgan, R. Aure, J. D. Stockero, J. A. Greenough, W. Cabot, O. A. Likhachev, and J. W. Jacobs, "On the late-time growth of the two-dimensional Richtmyer-Meshkov instability in shock tube experiments," J. Fluid Mech. **712**, 354–383 (2012).

[39] M. Lombardini and D. I. Pullin, "Startup process in the Richtmyer-Meshkov instability," Phys. Fluids **21**, 044104 (2009).

[40] G. Dimonte and P. Ramaprabhu, "Simulations and model of the nonlinear Richtmyer-Meshkov instability," Phys. Fluids **22**, 014104 (2010).

[41] W. T. Buttler, D. M. Oró, D. L. Preston, K. O. Mikaelian, F. J. Cherne, R. S. Hixson, F. G. Mariam, C. Morris, J. B. Stone, G. Terrones, and D. Tupa, "Unstable Richtmyer-Meshkov growth of solid and liquid metals in vacuum," J. Fluid Mech. **703**, 60–84 (2012).

[42] M. G. Probyn, R. J. R. Williams, B. Thornber, D. Drikakis, and D. L. Youngs, "2D single-mode Richtmyer-Meshkov instability," Physica D **418**, 132827 (2021).

[43] J. A. McFarland, J. A. Greenough, and D. Ranjan, "Investigation of the initial perturbation amplitude for the inclined interface Richtmyer-Meshkov instability," Phys. Scr. **T155**, 014014 (2013).

[44] K. O. Mikaelian, "Explicit expressions for the evolution of single-mode Rayleigh-Taylor and Richtmyer-Meshkov instabilities at arbitrary Atwood numbers," Phys. Rev. E **67**, 026319 (2003).

[45] Q. Zhang and W. Guo, "Universality of finger growth in two-dimensional Rayleigh-Taylor and Richtmyer-Meshkov instabilities with all density ratios," J. Fluid Mech. **786**, 47–61 (2016).

[46] Q. Zhang and W. Guo, "Quantitative theory for spikes and bubbles in the Richtmyer-Meshkov instability at arbitrary density ratios," Phys. Rev. Fluids **7**, 093904 (2022).

[47] M. M. Mansoor, S. M. Dalton, A. A. Martinez, T. Desjardins, J. J. Charonko, and K. P. Prestridge, "The effect of initial conditions on mixing transition of the Richtmyer-Meshkov instability," J. Fluid Mech. **904**, A3 (2020).

08 April 2024 03:52:15